Linear and Nonlinear Experiments in $\mathcal{PT}$-Symmetric Photonic Mesh Lattices

Martin Wimmer, Demetrios Christodoulides, and Ulf Peschel

Abstract Photonic mesh lattices provide a versatile experimental platform for studying light propagation in a discrete environment. By using standard telecommunication equipment it is possible to influence the evolution of light by actively modulating its amplitude and phase. Fiber components thus offer a ready to use solution for creating a $\mathcal{PT}$-symmetric optical network. Here, we analyze two classes of $\mathcal{PT}$-symmetric networks: those with local $\mathcal{PT}$ symmetry fulfilling the conditions of $\mathcal{PT}$ symmetry in each time step but not globally and those with global $\mathcal{PT}$ symmetry providing completely real eigenvalues. We investigate light propagation in these dissipative media in the linear and nonlinear regime and discuss nonlinear localization as well as the formation of soliton. Furthermore, Bloch oscillations are induced by an external phase modulation and are found to restore pseudo-Hermitian propagation.

1 Introduction

In this chapter, we discuss light propagation through a fiber optical network, which shares the same working principle as the Galton board [1] (see Fig. 1a). Originally proposed as a machine, where particles fall through multiple layers of scatterers, each deflecting the particles either to the left or to the right, it is a prime example for

M. Wimmer
Erlangen Graduate School in Advanced Optical Technologies (SAOT), Erlangen, Germany

Institute of Solid State Theory and Optics, Abbe Center of Photonics, Friedrich Schiller University Jena, Jena, Germany

D. Christodoulides
CREOL, College of Optics and Photonics, University of Central Florida, Orlando, FL, USA

U. Peschel (✉)
Institute of Solid State Theory and Optics, Abbe Center of Photonics, Friedrich Schiller University Jena, Jena, Germany
e-mail: ulf.peschel@uni-jena.de

D. Christodoulides, J. Yang (eds.), *Parity-time Symmetry and Its Applications*, Springer Tracts in Modern Physics 280,
https://doi.org/10.1007/978-981-13-1247-2_1

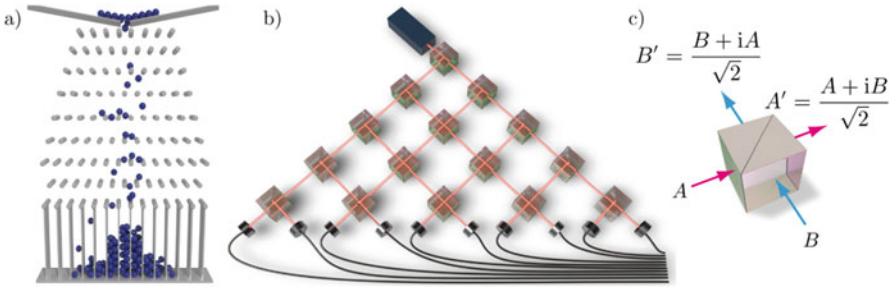

Fig. 1 Schematics of the classical and optical Galton board. (**a**) In case of the classical Galton board, a mechanical walker falls through multiple layers of scatterers, each deflecting the particle either to the left or to the right. (**b**) In the optical analogue, a laser beam is inserted into a pyramid of beam splitters. At each row of beam splitter cubes, the laser beam is divided up into one part going to the left and another going to the right. Photodetectors record the final intensity distribution. (**c**) The output of a standard 50/50 beam splitter is given by the superposition of both input fields, where the reflected path is phase shifted

Random Walks [2]. This stochastic process applied to classical particles reveals a diffusive motion, which is not time reversible. By replacing the mechanic particles by photons and the scatterers by beam splitters, a so-called optical Galton board is realized [3] (see Fig. 1b). Although the idea is the same, interestingly the optical version features a fast ballistic spreading [4] and a reversible evolution [5], providing an interesting ansatz for quantum mechanical search algorithms [6]. In the following, we present an implementation of the optical Galton board, which relies on fiber amplifiers for compensating losses. Therefore, the optical Galton board is discussed in terms of classical optics based on the propagation of coherent wave packets and their mutual interference [7]. At each beam splitter cube (see Fig. 1c), the incoming field amplitudes A and B transform into the fields A' and B' at the output according to

$$\begin{pmatrix} A' \\ B' \end{pmatrix} = \frac{1}{\sqrt{2}} \begin{pmatrix} 1 & i \\ i & 1 \end{pmatrix} \begin{pmatrix} A \\ B \end{pmatrix}, \tag{1}$$

where in this notation the reflected parts acquire a phase shift of $\pi/2$. As amplifiers and classical optical states are used in this project, the optical Galton board is called a Light Walk in order to distinguish it from Quantum Walks based on e.g. single photon states [8, 9] or atoms [5].

The main challenges of implementing the spatial Galton board are the growing number of components with increasing system size and the need for an active stabilization in order to observe a coherent propagation. A clever solution to both problems was demonstrated in [8], where time-multiplexing schemes are adapted to the challenge of realizing an optical Galton board. The working principle is not limited to a single spatial dimension, but even 2D Quantum walks could be realized based on this method [10]. In the following, we first want to discuss the

basics behind time multiplexing of Light Walks and afterwards we explain the experimental setup in detail. Finally, we present results on linear and nonlinear light evolution, even in presence of $\mathcal{PT}$-symmetrical potentials.

2 Light Walks via Time Multiplexing

The Galton board is a typical $1+1$ dimensional system, the rows of which can be interpreted as discrete time steps and the horizontal deflection of the walker as the position, which is discretized as well. For a time-multiplexed implementation of the optical Galton board, pulses are used instead of cw-signals. While in the standard arrangement all beam splitters of a single row are passed at the same time, in [8, 11] a time delay between each beam splitters is introduced by shortening all paths going the left compared to the paths going to the right (compare red and blue paths in Fig. 2a). The system now evolves on two time scales: firstly, each row is separated from the next by the path length $\overline{L} = (L_1 + L_2)/2$ and secondly the length difference $\Delta L = L_1 - L_2$, with $L_1 > L_2$, separates two adjacent beam splitters of the same row. Instead of labelling every beam splitter by its individual row m and column n, it is now possible to identify each beam splitter by a single parameter, which is the arrival time

$$T_{arrival} = \overline{T}m + \frac{\Delta T}{2}n. \tag{2}$$

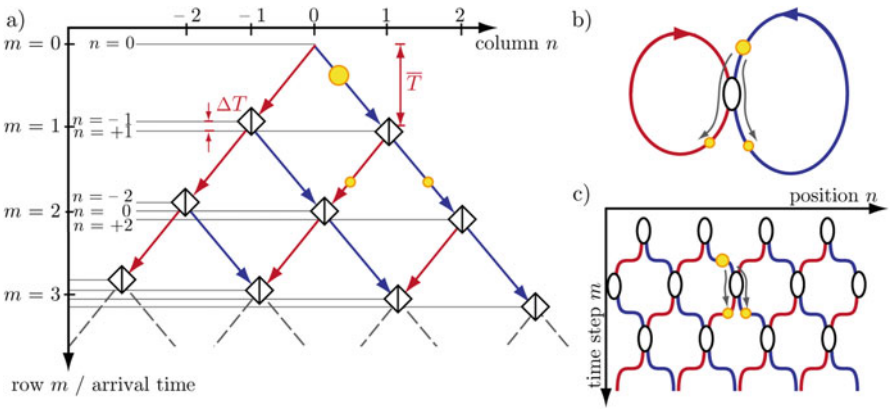

Fig. 2 Time multiplexing used to realize the optical Galton board. (**a**) Coding the spatial distribution of light pulses (yellow circles) by their arrival time: By shortening paths to the left (red), an artificial length difference is introduced, which attributes to each beam splitter in row m and column n a unique arrival time given by Eq. (2). Large time steps separate different rows, while small time steps separate pulses of the same row, but of different columns. (**b**) The pyramid is then reduced to two fiber loops of different length and a 50/50 fiber coupler. Each roundtrip in the short (long) loop equals a step to the left (right). The introduction of the length difference is not altering the dynamics through the pyramid. (**c**) Equivalent mesh lattice consisting of 50/50 fiber couplers. For a better visualization, the length difference between red and blue paths is ignored, since it does not influence the evolution

Here, we introduced the average propagation time $\overline{T}$ and the time difference ΔT between both optical paths. By creating the length imbalance between the short paths to the left and the long paths to the right, a dimensional reduction from 1 + 1D to a single temporal dimension is carried out, which has a crucial impact on the experiment: Not only the coordinate system of the optical Galton board is conflated, but instead also the experiment can be simplified to a short and a long piece of optical fibers connecting the input and output of a 50/50 fiber coupler (see Fig. 2b). A pulse starting in the longer loop is split up at the fiber coupler into two smaller pulses, which propagate in the short and long loop, akin to pulses propagating to the left or right in the pyramid of beam splitters. After each roundtrip they reach the central coupler, where they split up again. While a path through the spatial implementation of the optical Galton board is given by a combination of steps to the left or right, this translates into a specific sequence of short and long loop roundtrips in the temporal implementation. In this sense, each roundtrip of the pulses corresponds to a time step m, and the difference in number of round trips through the long and short loop define the position n.

Obviously, based on time multiplexing only the two fiber loops and the beam splitter are needed, which is the first main advantage. In case of the Galton board [1] the accessible propagation length is limited by the rapidly growing size of the required apparatus. In contrast, the maximum number of round trips realized in the temporal version is restricted to the ratio $N = \overline{T}/\Delta T$ between the average roundtrip time and the time difference. If this limit is exceeded pulses start mixing with those of the previous round trip. In our experimental setup, an average loop length of 4 km is chosen and a length difference of about 45 m. In this case, the spatial size of the optical Galton board extends over approximately 90 positions.

A second advantage of the time multiplexing principle is the intrinsic stability of the setup. Due to the reduction to only three components, the same parts are passed again and again. As a necessary condition for interference, two pulses have to meet at the 50/50 coupler at the same time, which is only possible, if they propagate for the same number of roundtrips through the long and short loop, but do not necessarily pass the loops in the same order. In practice this means, that any fluctuations with a larger time scale than a single measurement, do not influence the evolution as all possible paths are affected in the same way.

3 Experimental Setup

However, in reality more than three components are needed for realizing a time-multiplexed version of the Galton board (see Fig. 3). In the supplementary material of [11–13] detailed descriptions of the experiment are provided. For each measurement, a seed pulse with a length of 25 ns is cut out of the signal of a DFB laser diode ($\lambda_{signal} = 1555$ nm) by a Mach-Zehnder modulator (MZM). For achieving high peak powers, the pulse is amplified by two erbium-doped fiber amplifiers (EDFA) and

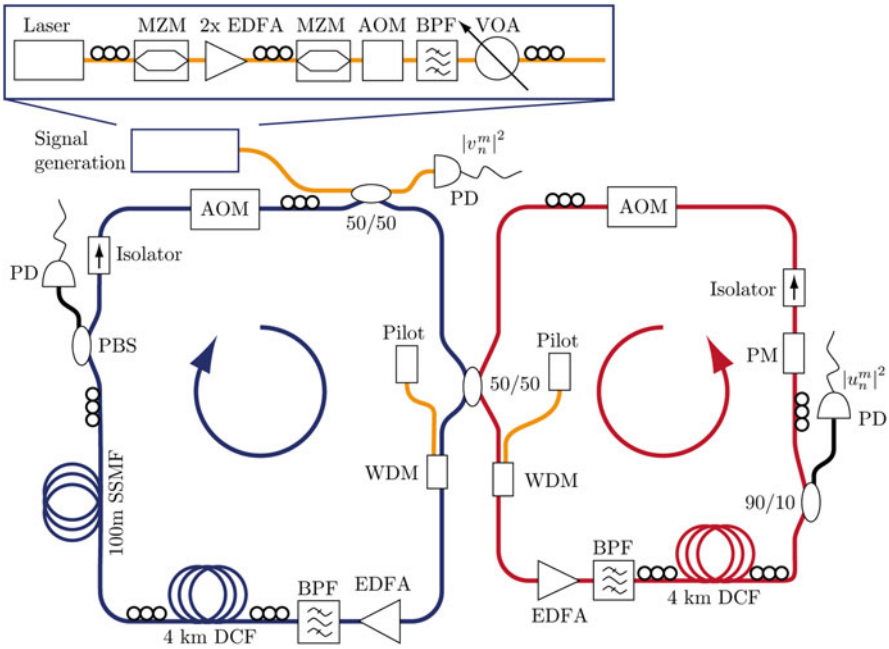

Fig. 3 Experimental setup consisting of the signal generation and the two optical fiber loops. The signal of a DFB laser diode is transformed into pulses by a Mach-Zehnder modulator (MZM) and amplified twice by erbium-doped fiber amplifiers (EDFA). Afterwards, the background is suppressed by another MZM and cleaned by a bandpass filter. The peak power is adjusted via a variable optical screw attenuator and an acousto-optical modulator (AOM). After inserting the seed pulse into the long loop via a 50/50 coupler, it passes a wavelength-division multiplexing coupler (WDM), which adds a pilot signal to each loop. All losses during one roundtrip are compensated by an EDFA followed by a tunable bandpass filter. 4 km of dispersion compensating fibers (DCF) provide a significant nonlinear phase shift already at low power levels. A polarizing beam splitter (PBS) and a phase modulator (PM) with an integrated polarizer in the short loop filter out a single polarization state. This state is adjusted via polarization controllers (denoted by three circles) at numerous positions. At the end of the loops, isolators block back reflections of the AOMs, which are used for a dynamic gain and loss modulation

afterwards reshaped again by a MZM in order to further suppress the dark signal. Before being injected into the long loop through a 50/50 coupler, the spectrum of the pulse is cleaned by a tunable bandpass filter and the peak power is adjusted by a variable optical attenuator and an acousto-optical modulator (AOM). Both fiber loops are built up in a nearly symmetric way, starting with an amplification stage. This consists of an EDFA in each loop, which is adjusted in such a way that any losses during one roundtrip are compensated. For avoiding transients and for adjusting the amplification rate, a continuous pilot signal at $\lambda_{pilot} = 1536$ nm is added via wavelength-division-multiplexing couplers (WDM). After the amplifiers, the pilot signal is filtered out by tunable bandpass filters before the pulses enter

4 km of dispersion compensating fibers (DCF). A DCF has a comparable small core size and thus a higher nonlinear coefficient compared to standard single mode fibers (SSMF) [14]. In combination with the long propagation distance of 4 km, this leads to nonlinear effects already at comparable low peak powers of 100 mW. The dominant nonlinear effect, which is observed in the experiment is self-phase modulation based on the Kerr effect. Based on fiber parameters provided in [14], it is estimated that a nonlinear phase shift of 2π is accumulated at a power level of about 300 mW within a single roundtrip [12]. Besides the two DCFs, a third spool of SSMF fiber is needed for balancing the length difference up to a remaining imbalance of 45 m. For monitoring the pulses, a 90/10 coupler is placed in the short loop after the fiber spools. In the longer loop, the injection coupler is also used for pulse monitoring. For adjusting the polarization in each fiber loop, the signal at the second output port of a polarizing beam splitter in the longer loop is minimized via manual polarization controllers. A phase modulator in the short loop determines the polarization state in the respective loop via an integrated polarizer. Optical isolators prevent any back reflections and the built up of stimulated Brillouin scattering. At the end of each loop, acousto-optical modulators (AOM) in zeroth order are used as intensity modulators. The transmission ratio of the AOM depends on the applied voltage, which is adjusted so, that only 50% of the pulse intensity passes, while the EDFA compensates for this additional loss. In this way, it is possible to either attenuate pulses by lowering the transmission ratio, or amplifying them by increasing the transmission.

4 Mathematical Description of the Evolution

As pulses are much too long to be influenced by the group velocity dispersion of the fiber they are completely characterized by complex amplitudes u_n^m and the pulses v_n^m in the long loop and short loop, respectively [11]. Each roundtrip the time step m of the system advances to $m + 1$, while the position n is either decreased for pulses in the short loop (going to the left) or increased for pulses in the long loop (propagating to the right). In combination with the matrix of a single 50/50 beam splitter in Eq. (1), this leads to the evolution equations [11]

$$u_n^{m+1} = \frac{1}{\sqrt{2}}\left(u_{n+1}^m + i\,v_{n+1}^m\right) \text{ and} \tag{3.1}$$

$$v_n^{m+1} = \frac{1}{\sqrt{2}}\left(v_{n-1}^m + i\,u_{n-1}^m\right). \tag{3.2}$$

The periodic arrangement of beam splitters in the optical Galton board reveals a unit cell, which covers two positions and two time steps. The periodicity itself is reflected in a band structure (see Fig. 4), which is derived by inserting a Floquet-Bloch ansatz [15].

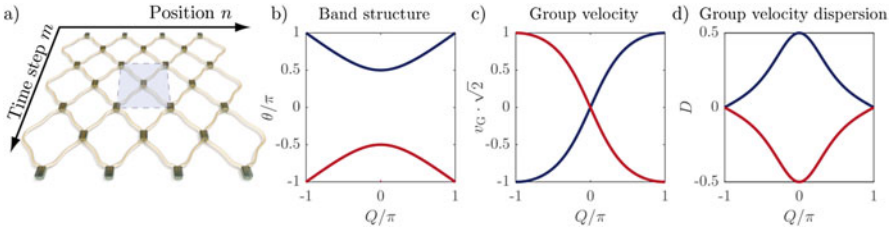

Fig. 4 Unit cell of the mesh lattice and the band structure. (**a**) The mesh lattice consists of unit cells covering two positions and two time steps. (**b**) The two-atom unit cell leads to a splitting of the band structure into two bands [15]. Due to the spatial and temporal discretization, the band structure is not only periodic in the Bloch momentum Q, but also in the propagation constant θ. (**c**) The group velocity vanishes at the center of the Brillouin zone and has maximum absolute values at the edges. (**d**) In the linear regime the second derivative of the dispersion relation determines the dispersive spreading of the wave packets [12, 16]

$$\begin{pmatrix} u_n^m \\ v_n^m \end{pmatrix} = \begin{pmatrix} U \\ V \end{pmatrix} e^{\frac{iQn}{2}} e^{-\frac{i\theta m}{2}} \tag{4}$$

into a double step of the evolution equations (3.1 and 3.2). The resulting dispersion relation

$$\cos\theta = \frac{1}{2}(\cos Q - 1) \tag{5}$$

connects the propagation constant θ with the Bloch momentum Q. As the evolution proceeds in discrete round trips, the band structure is not only periodic in the Bloch momentum Q but also in the propagation constant θ.

A specific point of the dispersion relation is excited by starting with a train of pulses with a Gaussian envelope in one of the loops. In the next round trip when pulses have distributed over both loops amplitudes and phases are tuned according to the desired eigenstate $(U, V)^{\mathrm{t}}$ [12]. However, the task of creating a Gaussian distribution is non-trivial, as the system loses its intrinsic stabilization, if an externally generated pulse sequence is inserted into one of the loops. In this case, pulses may interfere, which did not pass the same number of components. As a consequence, the phase relation between different pulses is no longer fixed and unpredictable fluctuations from one realization to the next may occur. However, it is possible to create internally a Gaussian distribution by blocking every second time step one of the two fiber loops [11]. The resulting evolution equations

$$u_n^{m+2} = \frac{1}{2}\left(u_{n+2}^m + iv_{n+2}^m + iv_n^m - u_n^m\right) \text{ and} \tag{6.1}$$

$$v_n^{m+2} = \frac{1}{2}\left(v_{n-2}^m + iu_{n-2}^m + iu_n^m - v_n^m\right). \tag{6.2}$$

then simplify to a discretized diffusion equation (e.g. if v_n^m is blocked):

$$u_n^{m+2} = \frac{1}{2}\left(u_{n+2}^m - u_n^m\right) \text{ and} \tag{7.1}$$

$$v_n^{m+2} = \frac{i}{2}\left(u_{n-2}^m + u_n^m\right), \tag{7.2}$$

the solution of which is known to be Gaussian for an initial single site excitation. Additional accumulations of phases and drifts of the center-of-mass can be avoided by blocking long and short loop in an alternating way every second time step. At the end, a wave packet is produced in each loop with a Gaussian envelope, where in a final step the phase and amplitude is adjusted through the modulators.

5 Creation of a $\mathcal{PT}$-Symmetric Potential

In their seminal work [17] on $\mathcal{PT}$-symmetric Hamiltonians, Bender and Boettcher considered a one-dimensional Schrödinger equation

$$i\hbar\frac{\partial}{\partial t}\psi(x,t) = -\frac{\hbar^2\partial^2}{2m\partial x^2}\psi(x,t) + V(x)\psi(x,t), \tag{8}$$

which is invariant under simultaneous time reversal $\mathcal{T}$ and inversion of space $\mathcal{P}$, setting up a symmetry condition for the potential

$$V(x) = V^*(-x). \tag{9}$$

Ten years later, the criterion above in Eq. (9) was transferred to the optical regime, where the refractive index distribution $n(x) = n_R(x) + in_I(x)$ replaces the potential $V(x)$ [18]. Consequently, a system fulfills $\mathcal{PT}$ symmetry, if the refractive index obeys the two conditions

$$n_R(x) = n_R(-x) \text{ and } n_I(x) = -n_I(-x) \tag{10}$$

simultaneously. The first successful realization of these symmetry conditions via two coupled waveguides was reported in [19]. While the sign of $n_I(x)$ distinguishes between an amplifying active medium ($n_I(x) < 0$) and a lossy medium ($n_I(x) > 0$), it is also possible to avoid any amplification by symmetrically distributing minor and major losses, e.g. by introducing bending losses in waveguide arrays [20, 21] or by adding absorbing layers [19, 22]. In such systems a global loss can be scaled out, leaving regions of amplification and attenuation [23]. However, the presence

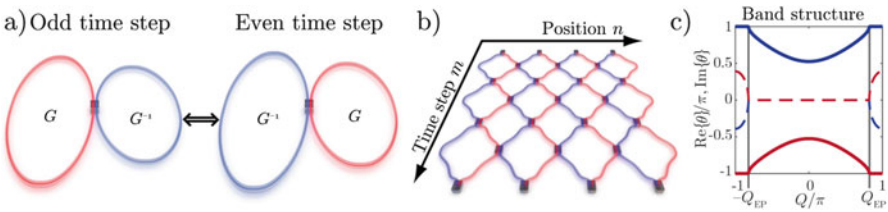

Fig. 5 Creation of an antisymmetric gain and loss distribution. (**a**) At odd time steps the long loop is amplified and the short loop attenuated, a situation, which is reversed for even time steps. (**b**) This alternating amplitude modulation corresponds to a mesh lattice with gain and loss waveguides, which are coupled at discrete time steps. (**c**) Exceptional points (EP) separate the complex part of the band structure from the real valued central part. At the EPs, the eigenvalues and eigenvectors of the system merge. The dash-dotted lines denote the imaginary part of the band structure

of a global loss limits the applicability, since the propagation length of optical signals is reduced. It also renders nonlinear experiments virtually impossible as the action of optical nonlinearities soon becomes negligible. Active systems like doped micro-ring cavities [24, 25] require a more stringent choice of materials, which is traded in for an avoidance of unnecessary losses. In optical fiber networks, commercially available amplifiers provide a convenient solution to this problem. We use a combination of amplitude modulators for dynamical gain and loss regulation and EDFAs for a static compensation of any damping [26–28]. The required symmetric real part of the refractive index distribution is on the other side realized by an appropriate phase modulation.

Starting with the imaginary part of the refractive index, an antisymmetric distribution is achieved by amplifying one loop by G and attenuating the other in a balanced way by $1/G$, which results in the evolution equations

$$u_n^{m+1} = \frac{\sqrt{G^{\pm 1}}}{\sqrt{2}} \left(u_{n+1}^m + i v_{n+1}^m \right) \text{ and} \tag{11.1}$$

$$v_n^{m+1} = \frac{\sqrt{G^{\mp 1}}}{\sqrt{2}} \left(v_{n-1}^m + i u_{n-1}^m \right). \tag{11.2}$$

After each time step, the gain and loss distribution is inverted (denoted by $\pm$), corresponding to the creation of temporally discretized coupled waveguides with gain and loss [26] as depicted in Fig. 5. A reflection of space requires at the same time an exchange of amplification and attenuation in order to restore the original lattice. In this sense, $\mathcal{PT}$ symmetry is already fulfilled by the sole imaginary part of the potential, however the resulting dispersion relation

$$\cos\theta = \frac{1}{2} \left(\cos Q - \cosh\gamma \right), \tag{12}$$

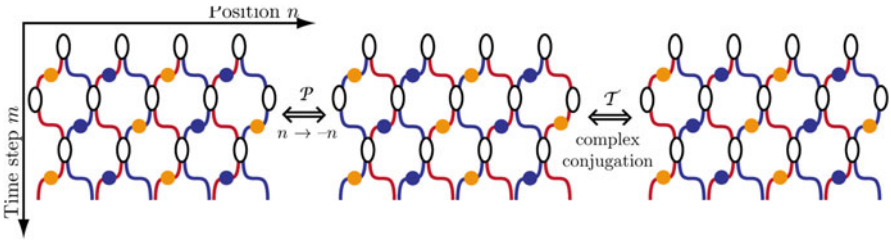

Fig. 6 Symmetry operations of the $\mathcal{PT}$ symmetric mesh lattice including the phase modulation. Parity symmetry leads to a reflection of space, which is equal to mirroring the lattice about a vertical line. Time inversion flips the lattice about the horizontal axis and adds complex conjugation, which is equal to an exchange of gain and loss. To demonstrate that those symmetries are still present in the case of phase modulation we have assumed the operation of a phase modulator in one of the loops. The phase modulation is denoted by blue ($-\varphi_0$) and yellow circles ($+\varphi_0$)

with $\gamma = (\ln G)/2$, shows complex eigenvalues at the edge of the Brillouin zone (see Fig. 5c). These zones are separated from a completely real valued region by exceptional points at

$$Q_{\mathrm{EP}} = \pm \arccos\left(2 + \cosh\gamma\right), \tag{13}$$

where not only the eigenvalues but even the eigenstates merge [29]. The resulting propagation is dominated by the exponential increase of power due to the complex eigenstates (see Fig. 9 third column).

In order to establish full $\mathcal{PT}$ symmetry in the whole Brillouin zone, it is mandatory to include also a phase modulation, which is equivalent to a symmetric real part of the refractive index. Since the gain and loss alternates with each lattice site thus realizing an antisymmetric potential, a symmetric phase modulation

$$\varphi(n) = \begin{cases} +\varphi_0, & \mathrm{mod}\,(n+3,4) < 2 \\ -\varphi_0, & \mathrm{else} \end{cases} \tag{14}$$

is needed with a periodicity of four spatial positions [26] (see Fig. 6). Eq. (14) is experimentally implemented via a phase modulator in the short loop

$$u_n^{m+1} = \frac{\sqrt{G^{\pm 1}}}{\sqrt{2}}\left(u_{n+1}^m + i\,v_{n+1}^m\right) e^{i\varphi(n)}, \tag{15.1}$$

$$v_n^{m+1} = \frac{\sqrt{G^{\mp 1}}}{\sqrt{2}}\left(v_{n-1}^m + i\,u_{n-1}^m\right). \tag{15.2}$$

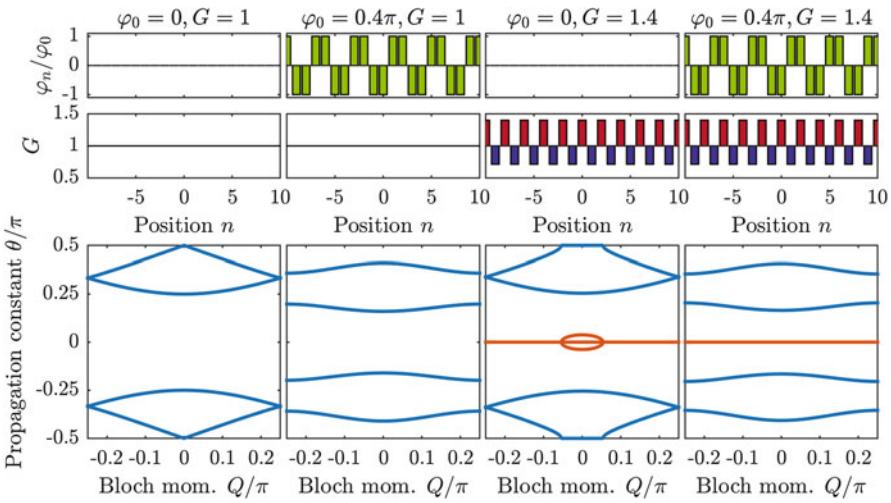

Fig. 7 Band structure of the $\mathcal{PT}$-symmetric lattice. In the case of a passive lattice as shown in the first column, the band structure is completely real valued. Applying a phase modulation increases the size of the unit cell, which leads to a splitting of the dispersion relation into four bands in total (second column). When complex valued (imaginary part is shown in red) and features exceptional points. In the case of a combined amplitude and phase modulation, the band structure is completely real valued again (fourth column). Compared to Figs. 4 and 5, the Floquet-Bloch ansatz in Eq. (16) is used, which leads to a backfolding of the band structure about the horizontal axis

For deriving the band structure (see Fig. 7) [15]

$$\cos 2\theta = -\frac{1}{2}\cos\varphi_0 \cosh 2\gamma \pm \frac{1}{2}\sqrt{\cos^2\varphi_0 \cosh^2 2\gamma + \frac{1}{2}\left[\cos 4Q - \cosh 4\gamma - 4\cos^2\varphi_0 + 4\right]}$$

of this lattice, a Floquet-Bloch ansatz

$$\begin{pmatrix} u_n^m \\ v_n^m \end{pmatrix} = \begin{pmatrix} U \\ V \end{pmatrix} e^{\frac{iQn}{4}} e^{-\frac{i\theta m}{2}} \tag{16}$$

with an increased spatial periodicity of four lattice sites is chosen. Due to the increased size of the unit cell, the original two bands split up in four. In absence of gain and loss ($G = 1$), the pulse spreads while maintaining a constant power level. However, for gain/loss values exceeding the PT threshold, the band structure is complex again (see Fig. 8). The increase and decrease of the phase for pairs of

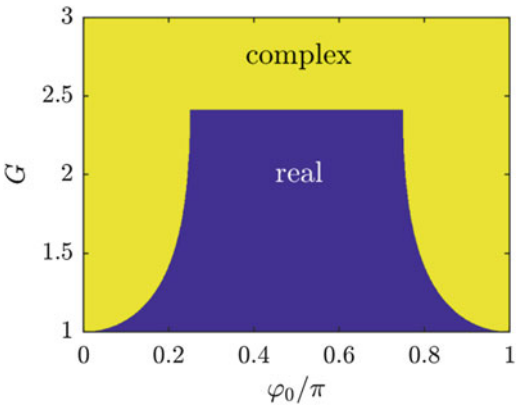

Fig. 8 $\mathcal{PT}$ threshold of the mesh lattice. Even when combining amplitude and phase modulation, $\mathcal{PT}$ symmetry does not guarantee a real-valued dispersion relation. Only below a critical value of the amplification G, the band structure is real, while above it has complex parts. The figure is adapted from the supplementary material accompanying [26]

waveguides leads to an effective decoupling to neighboring pairs and a reduced spreading compared to the passive lattice (see Fig. 9 second column).

6 $\mathcal{PT}$ Bloch Oscillations

Besides the real space propagation in Fig. 9, which illustrated the effects of a complex, but also proves the existence of a completely real valued band structure, further details about the shape of the dispersion relation are revealed by studying Bloch oscillations [11, 22, 28, 31]. The original idea of Bloch [32, 33] goes back to the motion of charge carriers in a crystalline material. In contrast to electrons in free space, charge carriers in a crystalline material cannot propagate freely, but instead their motion is dictated by the underlying band structure [34]. Therefore, by applying an electric field, charge carriers perform Bloch oscillations, which are a mirror image of the periodic band structure. In our optical system, electrical fields can be mimicked by linearly increasing phase gradients [11, 28] reminiscent to a refractive index gradient in waveguide arrays [35, 36].

For convenience we increase the induced phase in one of the loops in each time step

$$u_n^{m+1} = \frac{\sqrt{G^{\pm 1}}}{\sqrt{2}} \left(u_{n+1}^m + i\, v_{n+1}^m \right) e^{i\alpha m} \text{ and} \tag{17.1}$$

$$v_n^{m+1} = \frac{\sqrt{G^{\mp 1}}}{\sqrt{2}} \left(v_{n-1}^m + i u_{n-1}^m \right), \tag{17.2}$$

by a fixed amount α , a scheme, which is equivalent to a transverse modulation as demonstrated in [37]. Compared with a modulation in each transverse step n requiring a temporal resolution of $\Delta T \approx 200$ ns, the necessary band width of the

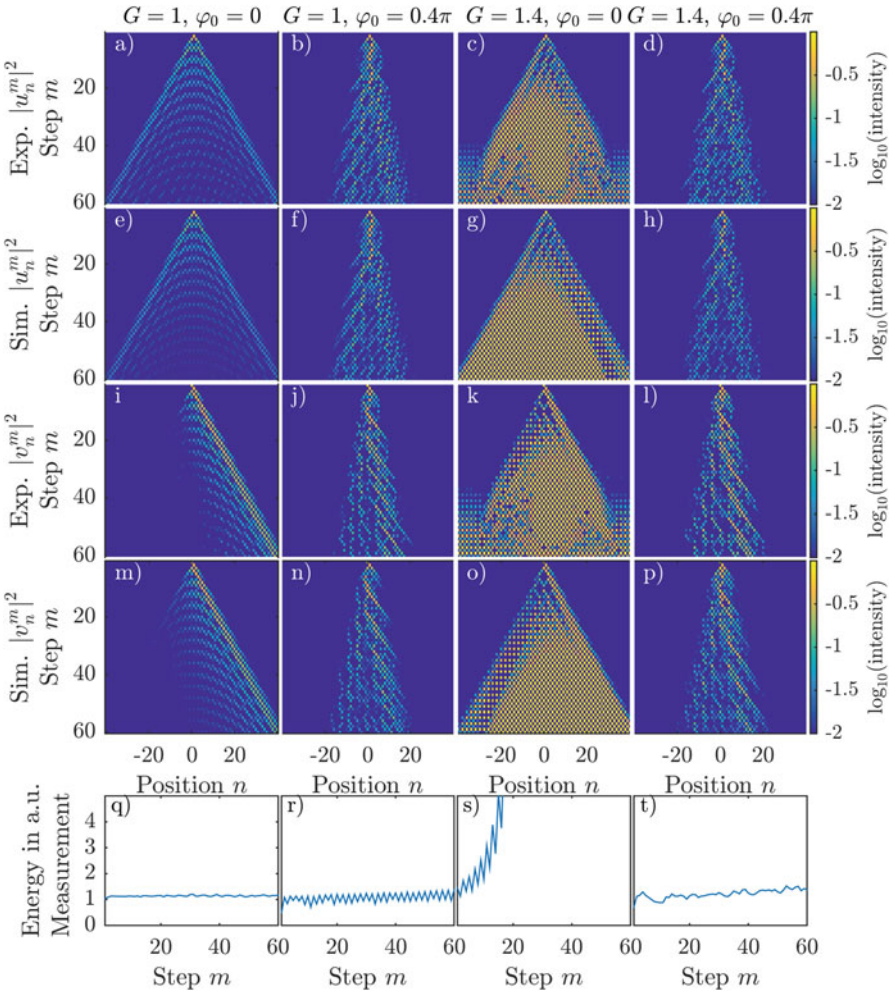

Fig. 9 Experimental and numerical propagation dynamics through the $\mathcal{PT}$ lattice. In absence of any modulation, the pulse distributions in both loops exhibit a classical Light Walk pattern [11] (see first column). By applying the phase potential in Eq. (14), waveguides are pairwise decoupled from each other, which reduces the spreading of a single lattice site excitation (second column). In the presence of a pure amplitude modulation, the complex band structure is reflected in an exponential increase in power (third column). The combination of both modulations restores $\mathcal{PT}$ symmetry for the whole band structure, and as a result power stays on average constant (fourth column). In a)-p) the intensities in the short or long loop are depicted. In q)-t) the total power is shown. This figure is motivated by [26] and depicts results from [28]

electrical signal generator for controlling the phase modulator is much lower in case of a modulation along the evolution direction m amounting to $\overline{T} \approx 20\ \mu\text{s}$ only. It is also possible to transform the temporal gradient into a spatial gradient

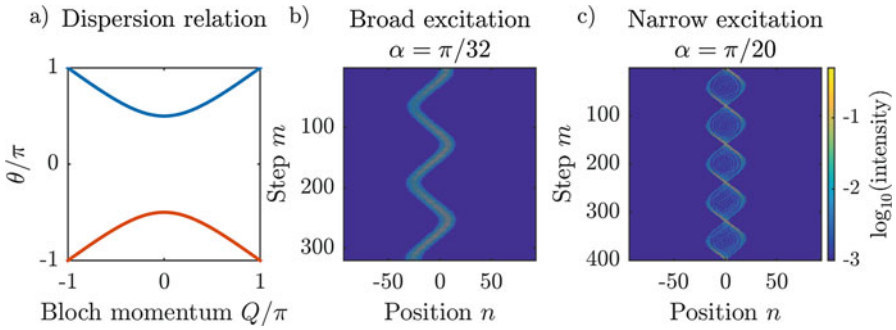

Fig. 10 Bloch oscillations in the passive lattice. By applying a phase gradient $\varphi(m) = m\alpha$, the Bloch momentum $Q = Q_0 + m\alpha/2$ of a spectrally narrow initial state is shifted for each time step. When reaching the edge of the Brillouin zone, the state performs a transition from one band to the other mediated by the Floquet-Bloch nature of the band structure. In real space, the continuous shift of the Bloch momentum is reflected in a periodic oscillation of the wave packet. The figure is adapted from [28] and shows experimental results

$$u_n^{m+1} = \frac{1}{\sqrt{2}}\left(u_{n+1}^m + i v_{n+1}^m\right) e^{\frac{i\varphi_0 n}{2}}, \tag{18.1}$$

$$v_n^{m+1} = \frac{1}{\sqrt{2}}\left(v_{n-1}^m + i u_{n-1}^m\right) e^{\frac{i\varphi_0 n}{2}}, \tag{18.2}$$

by choosing the ansatz

$$u_n^m = \widetilde{u}_n^m e^{-\frac{i\varphi}{2}nm} e^{\frac{im^2\varphi}{4}} e^{-\frac{im\varphi}{4}}, \tag{19.1}$$

$$v_n^m = \widetilde{v}_n^m e^{-\frac{i\varphi}{2}nm} e^{\frac{im^2\varphi}{4}} e^{-\frac{im\varphi}{4}}, \tag{19.2}$$

which however requires a spatial phase gradient in each loop.

Starting with a Gaussian distribution and in absence of gain and loss ($G = 1$), the wave packet performs classical Bloch oscillations (see Fig. 10b). This behavior can be explained by analyzing the evolution of the Bloch wave amplitudes of the system based on the ansatz $u_n^m = \widetilde{u}_m \exp(iQn)$ and $v_n^m = \widetilde{v}_m \exp(iQn)$.

If we assume that these amplitudes evolve from step m to step $m + 1$ by accumulating a phase $\widetilde{u}_{m+1} = \widetilde{u}_m \exp(i\theta(m))$ and $\widetilde{v}_{m+1} = \widetilde{v}_m \exp(i\theta(m))$, the dispersion relation

$$\cos\left(\frac{\theta}{2} + \frac{\alpha m}{2}\right) = \frac{1}{\sqrt{2}} \cos\left(\frac{Q}{2} + \frac{\alpha m}{2}\right) \tag{20}$$

is formally identical to that of a homogenous lattice (see Eq. 5) except for an m-dependent shift in absolute phase, and more importantly in the position in the

Brillouin zone. Each time step, the effective Bloch momentum Q is increased by $\alpha m/2$. When starting at the center of the Brillouin zone $Q_0 = 0$, the edge is reached at $\alpha m/2 = \pi$. At this point, the Floquet-Bloch nature of the system mediates a transition from one band to the other, since the upper left (right) and lower right (left) points of the dispersion relation are pairwise degenerate (see Fig. 10). As a result, the wave packet reenters the Brillouin zone from the opposite site. However, at the same time it changes to the other band and continues there the Bloch oscillation until it reaches again the edge of the Brillouin zone.

For sampling the Brillouin zone via Bloch oscillations we expect the most interesting effects to occur for a band structure consisting of real and complex valued sections being connected by exceptional points at $\pm Q_{EP}$. This is already realized for pure amplitude modulation ($G \neq 1, \varphi_0 = 0$), which we will consider in the following. On its way through the Brillouin zone the wave packet has to pass not only the region of complex eigenvalues but also two exceptional points. In higher dimensions, instead of passing the EP it is also possible to encircle it, which leads to a non-adiabatic transition of the excitation from one band to the other as theoretically discussed in [38] and experimentally demonstrated in [39]. At each exceptional point the two bands merge and respective eigenstates are coupled. In 1D, when crossing such pair of EPs confining a complex section of the band structure the wave packet is not only amplified, but a part of its energy is also transferred to the other band. In real space (see Fig. 11) this splitting is

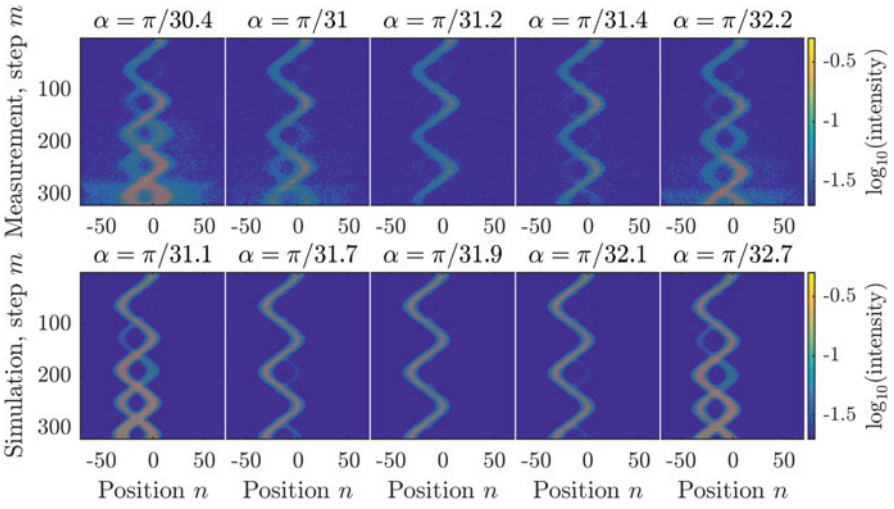

Fig. 11 $\mathcal{PT}$ Bloch oscillations. In presence of $\mathcal{PT}$ amplitude modulation ($G \approx 1.1$), the band structure is partially complex valued and features two exceptional points. The complex propagation constants lead to an increase in power during each Bloch oscillation, while at the exceptional points, a secondary branch is emitted into the opposite direction. However, for a set of magic gradients (here at $\alpha \approx \pi/31.2$), the propagation is pseudo-Hermitian and any emission of a second branch is strongly suppressed. These measurements support the theoretical results from [31] and are shown in [28]

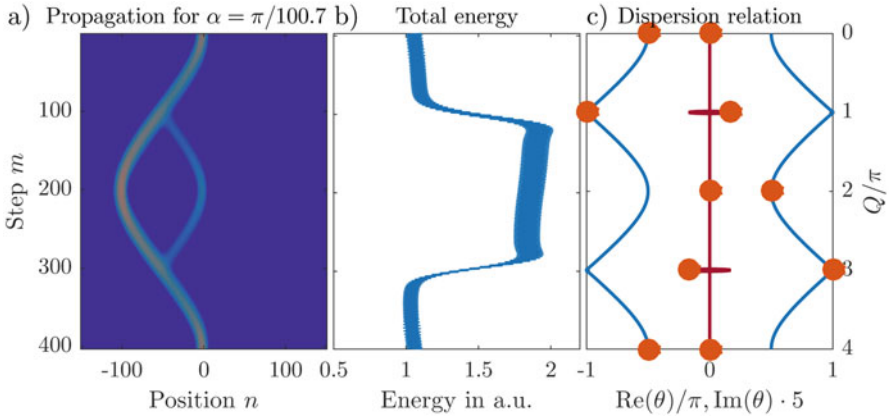

Fig. 12 Detailed numerical analysis of a single $\mathcal{PT}$ Bloch oscillation**. (a)** Real space propagation of a Bloch oscillation in presence of the $\mathcal{PT}$ amplitude modulation ($G = 1.1$). During the first half of the Bloch oscillation, the total energy shown in (**b**) increases, when the wave packet passes the complex region of the band structure. During the second half, the intensity drops again to the original value. (**c**) Dispersion relation with states of the wave packet (orange circles) for specific points during the propagation. Interestingly, even when passing the EPs, not all information is lost but instead the wave packet moves to the other band. The real part of the dispersion relation is shown in blue and the imaginary part in red. The imaginary part is stretched by a factor of five for better visibility

accompanied by the emission of a secondary branch, which counter propagates to the original one. As the wavenumber shift is the same for both bands, the two wave packets meet again at the exceptional points and power is redistributed between the bands. In some cases one of the branches is completely cancelled by destructive interference (see Fig. 12). By performing experimental and numerical sweeps over different Bloch gradients α this fascinating phenomenon is further investigated (see Fig. 11). As theoretically predicted in [31] the emission of the secondary branch is suppressed and the amplification and attenuation during the complex regions of the band structure is exactly balanced for some magic gradients. In simulations an even wider interval of Bloch gradients are accessible, which show a set of such magic gradients, for which the propagation is pseudo Hermitian (see Fig. 13).

7 Bloch Oscillations in the Local $\mathcal{PT}$-Symmetric Lattice

In the previous sections, two different approaches were described for achieving a pseudo-Hermitian propagation, where the total power is on average constant. First a spatial phase modulation was introduced, which completes the amplitude modulation in terms of the symmetry requirements of $\mathcal{PT}$ symmetry in Eq. (10). In the previous section another method based on Bloch oscillations was discussed,

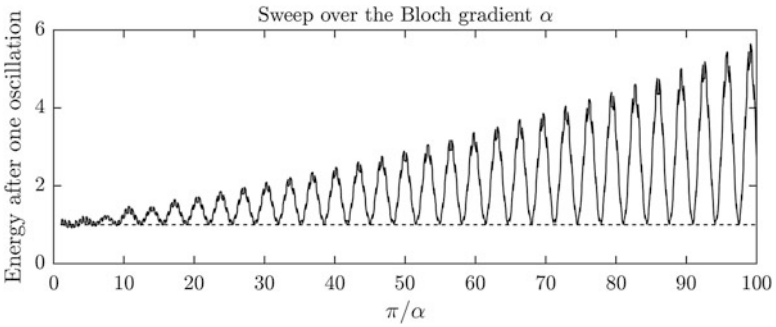

Fig. 13 Numerical parameter sweep of the Bloch gradient. For each Bloch gradient α, a single Bloch oscillation over $\approx 4\pi/\alpha$ time steps is simulated. The initial energy at the first time step is normalized to one, which is marked by the horizontal dashed line as a guide to the eyes. The solid curve depicts the energy after a full Bloch oscillation, which takes the initial value for the magic gradients (intersection points of the dashed and solid curve). By scaling the horizontal axis with the reciprocal value π/α, reveals a nearly equidistant spacing of the magic gradients. The amplification and attenuation rate is set to $G = 1.1$

where special gradients also lead to a pseudo-Hermitian propagation even in absence of the $\mathcal{PT}$ phase modulation. Therefore, the question remains, whether there are simpler ways of realizing a dissipative system with real eigenvalues. In the previous sections, the distribution of amplification and attenuation between the two fiber loops was alternating after each round trip for creating coupled waveguides with gain and loss. However, with respect to experiments, a static distribution of gain and loss is more relevant: A small maladjustment of the amplification rates of the EDFAs either leads to an exponential increase or decrease in power. While in reality, the EDFAs are precisely enough adjusted, so that hardly a change in the total power is visible, in the following a provoked imbalance is discussed. In this case, the long loop is amplified by G and the short loop is attenuated by G^{-1} according to

$$u_n^{m+1} = \frac{1}{\sqrt{2G}} \left(u_{n+1}^m + i v_{n+1}^m \right) \text{ and} \tag{21.1}$$

$$v_n^{m+1} = \frac{\sqrt{G}}{\sqrt{2}} \left(v_{n-1}^m + i u_{n-1}^m \right). \tag{21.2}$$

As a result, pulses moving to the right on the lattice are amplified, while pulses to the left are attenuated.

Also this lattice formally fulfills the requirements of $\mathcal{PT}$ symmetry in Eq. (9) for each time step (see Fig. 14), the dispersion relation

$$\cos\theta = \frac{1}{2} \left[\cos\left(Q + i\gamma\right) - 1 \right] \tag{22}$$

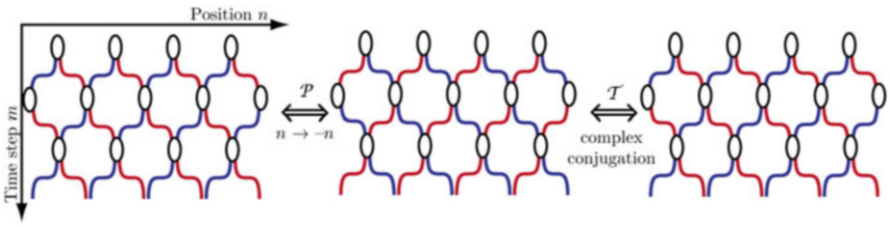

Fig. 14 Symmetry operations of the local $\mathcal{PT}$-symmetric lattice. Similar to Fig. 6, symmetries are analyzed in the local $\mathcal{PT}$ -symmetric lattice: The parity operation requires a left-right flip of the lattice and time reversal complex conjugation. However, here the lattice is not symmetric with respect to an additional vertical flip ($m \to -m$) as for time reversal symmetry in the global $\mathcal{PT}$-symmetric case (see Fig. 6). Therefore, the lattice preserves $\mathcal{PT}$ symmetry for each instantaneous time step, but not globally

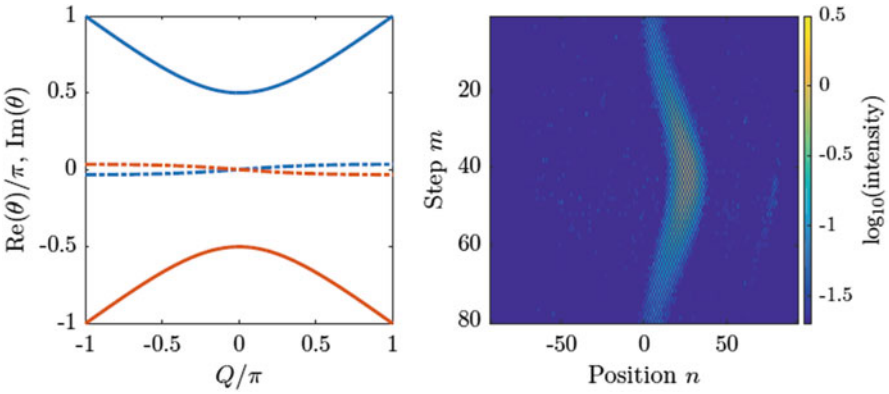

Fig. 15 Band structure of the local $\mathcal{PT}$ symmetric system and real space motion during a full Bloch oscillation**. (a**) The band structure consists of two bands, where only for $Q = 0$, the imaginary part of θ (dash-dotted lines) vanishes. The real part is shown as solid lines. (**b**) During one Bloch oscillation ($\alpha = \pi/30$), the wave packet is amplified ($G = 1.1$), while it propagates along the gain direction. At the edge of the Brillouin zone, it reenters the band structure from the opposite site and changes to the other band. Due to the symmetric imaginary part, the amplitude decays again, when the wave packet returns to its initial position. Figure is adapted from [28]

of this lattice shows complex eigenvalues over the complete Brillouin zone except at $Q = 0$ (see Fig. 15). Even by including the $\mathcal{PT}$ phase modulation, it is not possible to restore real eigenvalues. This highlights the circumstance that fulfilling $\mathcal{PT}$ symmetry does not guarantee completely real eigenvalues. Here, $\mathcal{PT}$ symmetry is fulfilled for each time step, however not for the global lattice when performing the combined operations for time reversal $\mathcal{T}$: $m \to -m$ and $G \to 1/G$ and parity $\mathcal{P}$: $n \to -n$. Therefore, this lattice is referred to as local $\mathcal{PT}$-symmetric [27].

Although the band structure of the lattice shows complex eigenvalues, it is possible to transform the system into a Hermitian counterpart by introducing reflecting

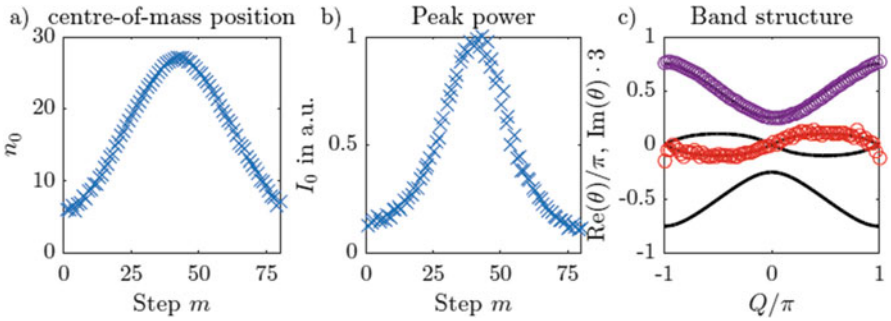

Fig. 16 Reconstruction of a complex band structure based on experimental results on Bloch oscillations. The center-of-mass motion and the evolution of the peak power is extracted by fitting a Gaussian distribution according to Eq. (23) to each row of the propagation in Fig. 15. (**a**) The derivative of the center-of-mass motion follows the group velocity of the system, which is in turn determined by the derivative of the dispersion relation (see Eq. (25)). (**b**) The increase of the amplitude each time step is determined by the imaginary part of θ (see Eq. (28)). (**c**) By evaluating both parameters, the real (violet) and imaginary part (red) of the dispersion relation is reconstructed. The amplification and attenuation rate is set to $G = 1.1$ and the Bloch gradient to $\alpha = \pi/30$. Figure is adapted from [28]

boundaries. In this case, any propagation in the amplified loop is limited by the finite system size, where at the edge the pulses are reflected from the gain direction into the loss one. Despite an initial amplification, no path can be constructed with an unbounded increase in power. Besides this illustrative explanation, also numerical calculations of the finite system indicate real eigenvalues.

In combination with Bloch oscillations an interesting question arises: On the one hand, the amplitude modulation leads to an amplification of pulses tending always into the same direction. On the other hand, applying the Bloch gradient forces wave packets to perform an oscillatory motion. In order to shed light on the question, which mechanism dominates, the temporal phase gradient $\varphi(m) = \alpha m$ is combined with a static amplitude modulation. The propagation of the wave packet starts as expected: The wave propagates analogously to the passive Bloch oscillation depicted in Fig. 15. However at the same time, the wave is amplified as it propagates into the direction of the gain loop. After half of the Bloch period, the Bloch oscillation forces the wave packet to propagate along the lossy direction back to its initial position, where it arrives without a change in the amplitude.

It is even possible to analyze systematically the position $n_0(m)$ and amplitude $A(m)$ of the wave packet at each time step for reconstructing the dispersion relation (see Fig. 16). For this purpose, a Gaussian curve

$$f(n) = Ae^{-\frac{(n-n_0)^2}{\sigma^2}} \tag{23}$$

is fitted to the pulse distribution in each time step. In a semi-classical picture of wave packet propagation, the center-of-mass of the wave packet estimated by n_0 moves at the group velocity

$$v_{\mathrm{G}} = \frac{\partial \theta(Q)}{\partial Q} \approx \frac{\partial n_0(m)}{\partial m}, \tag{24}$$

where $Q = Q_0 + m\alpha/2$. Consequently, the real part of the dispersion relation is given by the discrete summation over the center-of-mass motion

$$\theta_R(Q) = \int_0^{2\pi} dQ v_G(Q) \approx \sum\nolimits_{m=0}^{M} \frac{n_0\,(m+2) - n_0\,(m-2)}{4}. \tag{25}$$

within M time steps of a complete Bloch oscillation. The finite difference in Eq. (25) is evaluated at ± 2 due to the natural size of the unit cell covering two time steps. Complementary to the center of mass motion, the imaginary part of the propagation constant determines the evolution of the amplitude. After M time steps, the amplitude of an eigenstate

$$\psi = \begin{pmatrix} U \\ V \end{pmatrix} e^{iQm} e^{-i\theta_{\mathrm{R}} m} e^{i\theta_{\mathrm{I}} m} \tag{26}$$

is given by

$$|A(m)| = |A(0)| \prod\nolimits_{m=0}^{M} e^{\theta_I(Q(m))} = |A(0)| \exp\left(\sum\nolimits_{m=0}^{m} \theta_I\,(Q(m))\right). \tag{27}$$

In the measurement, the intensity of the wave packet is extracted by fitting the Gaussian distribution in Eq. (23). Therefore, the finite difference of the logarithm of the amplitude reveals the imaginary part of the propagation constant

$$\theta_I = \frac{\ln I\,(m+2) - \ln I\,(m-2)}{8}. \tag{28}$$

8 Nonlinear Light Propagation in the Fiber Network

On the one hand, linear light evolution through the lattice is already capable of depicting numerous phenomena like Bloch oscillations [22, 28, 31], unidirectional invisibility [26, 40–42] and the existence of trivial and topological $\mathcal{PT}$ defect states [20, 43–45]. On the other hand, the use of dispersion compensated fibers in the optical fiber network provides easy access to the nonlinear regime [12, 27]. For the optical Galton board, nonlinear effects were first theoretically studied in [46]. In experiments, the dominant nonlinear effect is the self-phase modulation (SPM) through each fiber loop. Already at comparable low peak powers of 300 mW a

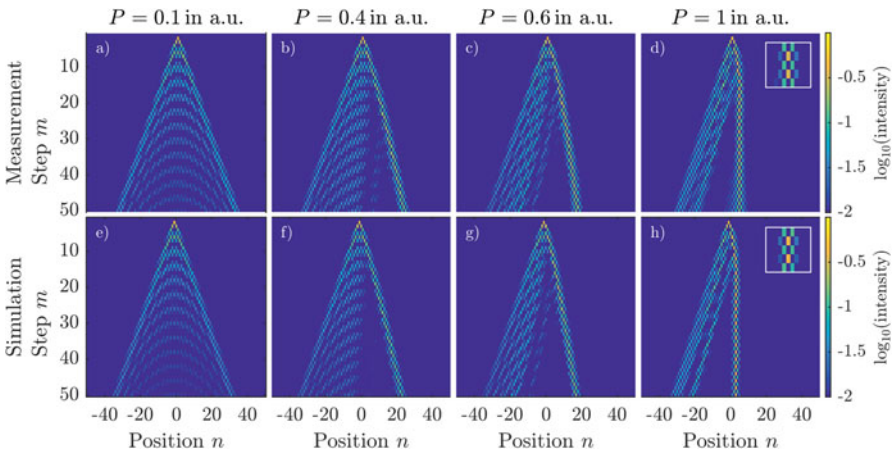

Fig. 17 Experimental observation of a Hermitian soliton in the double discrete mesh lattice. By increasing the initial power of the seed pulse, a soliton is formed, which is discretized in space and position. Figure is adapted from [27]

nonlinear phase shift of 2π is expected to accumulate within a single round trip, an effect which can be easily included in the evolution equations

$$u_n^{m+1} = \frac{\sqrt{G(m)}}{\sqrt{2}} \left(u_{n+1}^m + i\, v_{n+1}^m\right) e^{i\Gamma \left|u_{n+1}^m + i v_{n+1}^m\right|^2} e^{i\varphi(n)}, \tag{29.1}$$

$$v_n^{m+1} = \frac{\sqrt{G(m)}}{\sqrt{2}} \left(v_{n-1}^m + i u_{n-1}^m\right) e^{i\Gamma \left|v_{n-1}^m + i u_{n-1}^m\right|^2}. \tag{29.2}$$

In these measurements, the initial peak amplitude is varied via a screw attenuator and an AOM is used for an automatic parameter sweep.

We first discuss nonlinear evolution of the passive optical Galton board ($G = 1$) and $\varphi(n) = 0$. By increasing the power level of the initial seed pulse, the formation of a nonlinear wave is observed, which is bent towards the center of the Light Walk distribution (see Fig. 17). Compared to the initial propagation angle, the nonlinear wave propagates at a lower velocity as it is hindered by an increasing Peierls-Navarro potential [47, 48]. Light, which was originally located at the center of the Light Walk, is simultaneously repelled and shifted away from of the nonlinear wave.

This redistribution of intensities is mediated by the two band system: By starting with a single pulse, the complete Brillouin zone including both bands is excited. The effect of self-phase modulation now depends on the curvature of the respective band, which either leads to self-focusing (upper band) or defocusing (lower band) [16]. Between both bands, a diametric interaction takes place, which leads to a simultaneous attraction and repulsion [12]. At even higher peak powers, which correspond to a nonlinear phase shift of approximately 0.8π, the nonlinear

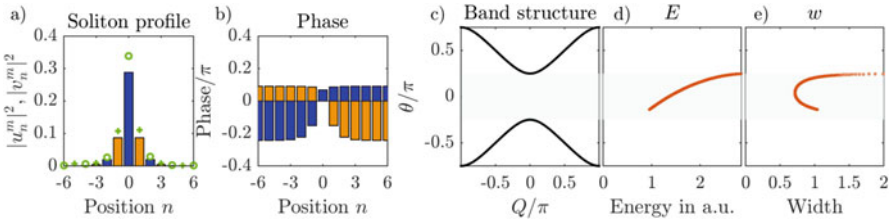

Fig. 18 Numerically determined soliton solutions. (**a**) Comparison between experimentally (crosses and circles) and numerically (bars) determined soliton profiles. The experimental data are extracted from time step $m = 25$. (**b**) Phase distribution across the soliton profile for the short and long loop. (**d**, **e**) Dependency of the soliton energy and width on the propagation constant. Figure is adapted from [27]

wave forms a soliton, propagating stable for approximately 45 time steps in the experiment. The soliton is not only discretized in space but even in time. As a result of the discretization, the main soliton pulse at the center cyclically splits up and reunites during two time steps.

Besides the experimental and simulated soliton formation and propagation, also numerical soliton solutions are found see (Fig. 18). The soliton solver is initialized with a Gaussian distribution for U_n and V_n with a $1/e$ width of 5 positions and an amplitude of 0.2. For a specific propagation constant θ_0 of the soliton within the band gap, the residual error

$$\delta f = \left\| f\left(\vec{v}\right) - \vec{v}\, e^{-i\theta} \right\| \tag{30}$$

after one time step is calculated. Here, $\vec{v} = (U_1, V_1, U_2, V_2, \ldots, U_N, V_N)^{\mathrm{t}}$ denotes a vector, which is constructed out of the soliton profile and f denotes the nonlinear evolution equations. The residual error is then minimized based on Newton's algorithm. For a propagation constant of $\theta = -0.2\pi$, the soliton solver initially converges within numerical precision. The complete branch of solitons is then calculated by choosing the last soliton solution as an initial guess for the soliton with a different propagation constant θ. For each solution, the width

$$w^2 = \frac{\sum_{n=-N_{max}}^{N_{max}} (n - n_0)^2 \left[|U_n|^2 + |V_n|^2\right]}{\sum_{n=-N_{max}}^{N_{max}} \left[|U_n|^2 + |V_n|^2\right]} \tag{31}$$

with

$$n_0 = \frac{\sum_{n=-N_{max}}^{N_{max}} n \left[|U_n|^2 + |V_n|^2\right]}{\sum_{n=-N_{max}}^{N_{max}} \left[|U_n|^2 + |V_n|^2\right]} \tag{32}$$

and energy

$$E = \sum_{n=-N_{max}}^{N_{max}} \left[|U_n|^2 + |V_n|^2 \right] \tag{33}$$

of the soliton are determined.

The stability of the soliton is numerically investigated by perturbing the solution $U_n \rightarrow U_n e^{i\delta_n}$ and $V_n \rightarrow V_n e^{i\delta_n}$ with an equally distributed phase noise δ_n. Below the center of the band gap $\theta_0 < 0$ solitons propagate stable, while above the band gap, even in absence of an initial noise the soliton decays into a stable solution [27]. Besides solitons with a maximum, which is maximum localized on a single lattice site, a second class of solitons is also found with symmetrically distributed maximum on two sites.

9 Solitons in the Local $\mathcal{PT}$ Symmetric Lattice

An interesting situation arises when nonlinearity is combined with a static amplification to the right and the attenuation of pulses propagating to the left, which was discussed before in terms of local $\mathcal{PT}$ symmetry. When injecting a low power pulse, an asymmetric Light Walk arises due to the gain/loss imbalance (see Fig. 19). However, the continuous amplification of the pulses travelling through the long loop (to the right in the optical Galton board) leads to an accumulation of nonlinear

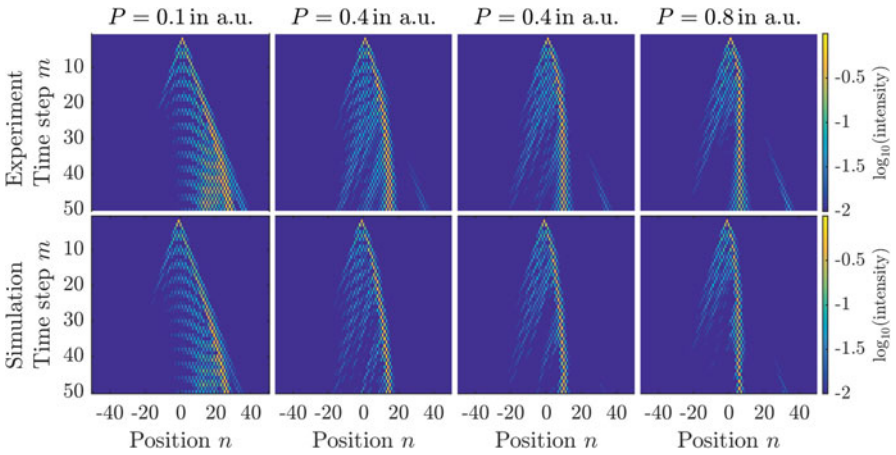

Fig. 19 Dissipative Light Walk in the local $\mathcal{PT}$-symmetric system. At low power levels, the Light Walk shows an asymmetric distribution due to the amplification in the long loop and the attenuation in the short loop ($G = 1.1$). For medium power levels, the initial amplification to the right is sufficient to form the double discrete soliton. The soliton maintains a constant power by equally propagating through the long and short loop. This figure is adapted from [27]

effects even in spite of the initial linear power level. As a consequence of the increase in power, a nonlinear wave is formed, which loses mobility due to its increasing peak power. It bends towards the center of the light walk distribution, where it finally forms a soliton, which manages to propagate in a balanced way through the gain and loss loops, so that no increase or decrease in power takes place. As this soliton on average experiences neither gain nor loss, it closely reproduces the features of its Hermitian counterpart thus forming a one-parameter family, a finding which could be confirmed by numerical simulations. This is different from localized solutions in other dissipative systems, which tend to form fixed point solutions [49], albeit exceptions like e.g. the cubic-quintic Ginzburg-Landau equation that are known to exist (see e.g [49–52].). In fact the directional distribution of gain and loss tends to stabilize the system, as any perturbation of the soliton is radiated away along the gain direction (see Fig. 20).

This internal power management of the soliton also provides the possibility of steering it through an additional global loss L in the evolution equations,

$$u_n^{m+1} = \frac{\sqrt{L}}{\sqrt{2G}} \left(u_{n+1}^m + i v_{n+1}^m\right) e^{i\Gamma \left|u_{n+1}^m + i v_{n+1}^m\right|^2}, \tag{34.1}$$

$$v_n^{m+1} = \frac{\sqrt{LG}}{\sqrt{2}} \left(v_{n-1}^m + i u_{n-1}^m\right) e^{i\Gamma \left|v_{n-1}^m + i u_{n-1}^m\right|^2}. \tag{34.2}$$

In the experiment, typically small gain/loss imbalances of $\gamma = \frac{(\ln G)}{2} \ll 1$ are investigated, where e.g. $G = 1.1$ and thus $\gamma \approx 0.05$. In this case, the real and imaginary parts of the dispersion relation ($\Gamma = 0$) are expanded in Taylor series

$$\mathrm{Re}\,\{\theta\} = \theta(Q)|_{\gamma=0} + \mathcal{O}\left(\gamma^2\right) \text{ and} \tag{35.1}$$

$$\mathrm{Im}\,\{\theta\} = \left.\frac{\partial \theta}{\partial Q}\right|_{\gamma=0} \gamma + \mathcal{O}\left(\gamma^3\right). \tag{35.2}$$

For a positive imaginary part of θ, the amplitude $A(m)$ of an eigenstate increases by

$$\left|\frac{A\,(m+1)}{A(m)}\right| = e^{\theta_{im}} \tag{36}$$

according to the Floquet-Bloch ansatz in Eq. (4). The increase in amplitude then has to overcome the global loss L per roundtrip, which yields with Eq. (35.2) the critical velocity

$$v_{crit} = \frac{\ln L}{\ln G}, \tag{37}$$

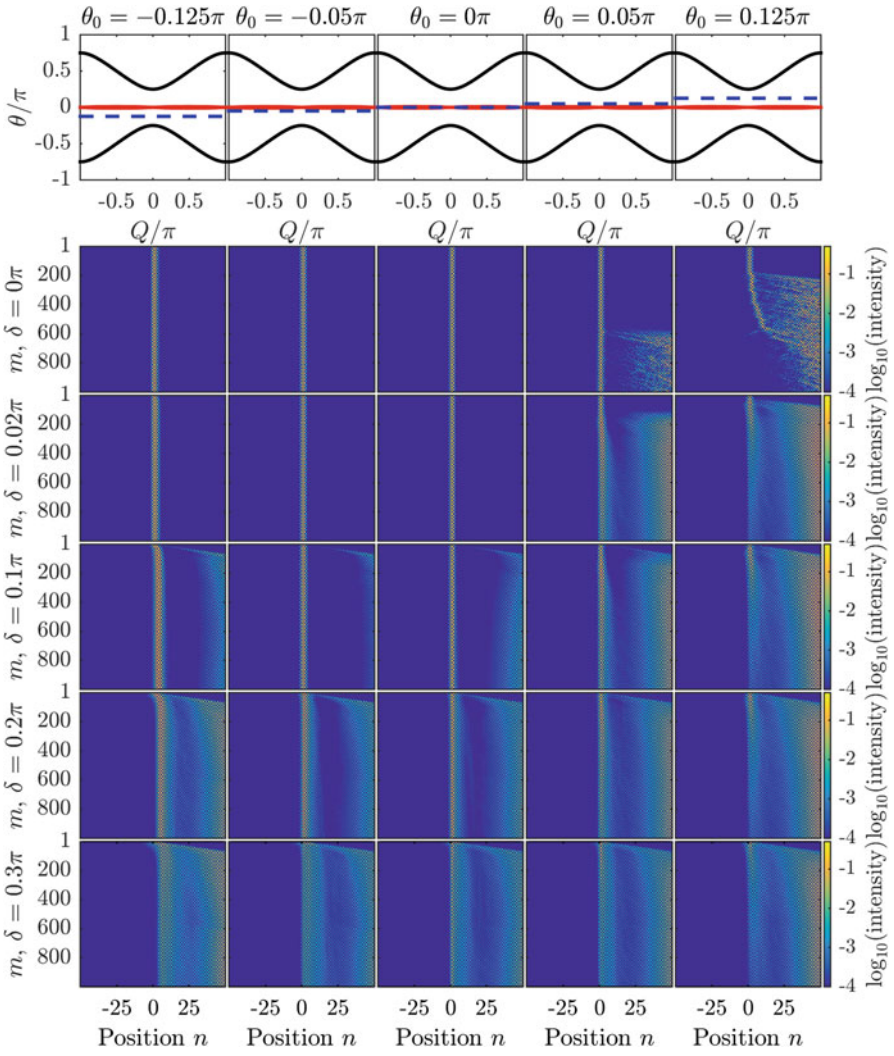

Fig. 20 Numerical test of the stability of dissipative solitons. The stability of the various solitons (different columns) of the local $\mathcal{PT}$-symmetric lattice ($G = 1.1$) is probed by different perturbations of the initial distribution $U_n' = U_n \exp(i\delta_n)$ and $V_n' = V_n \exp(i\delta_n)$ with a random phase noise δ_n (different rows of the figure), which is equally distributed between 0 and δ. The upper row displays the propagation constant of the soliton and its location in the band structure. For propagation constants $\theta_0 < 0$ (left three columns) the soliton is stable. In this case, noise is radiated into the direction of amplification, until it is absorbed at the boundary of the simulation domain. For $\theta_0 > 0$ (two columns on the right), the soliton either decays into a stable solution or vanishes completely. This figure is adapted from the supplementary material of [27]

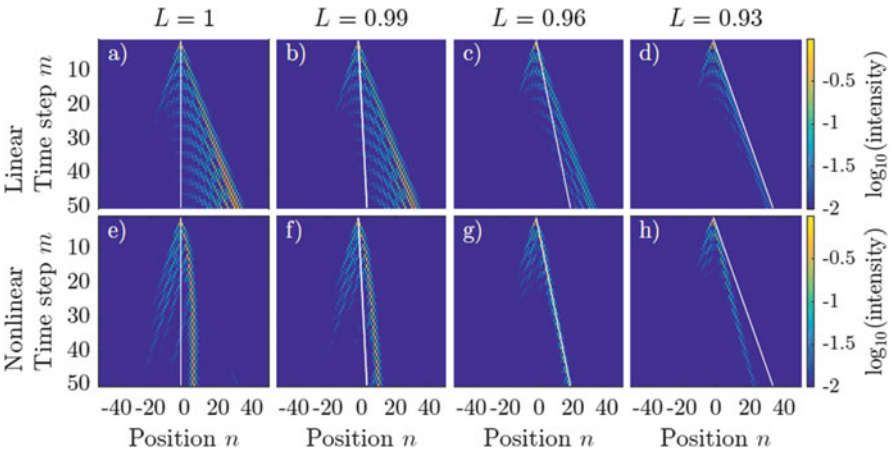

Fig. 21 Simulation of linear and nonlinear Light propagation through the local $\mathcal{PT}$-symmetric lattice with a global loss. In the linear regime, the critical velocity in Eqs. (34.1 and 34.2) separates the attenuated from the amplified parts. In the nonlinear regime ($\Gamma \approx 0.67\pi$), the same velocity is a good measurement for the soliton velocity. However, for large losses as $L = 0.93$ compared to the gain and loss imbalance of $G = 1.1$, the decreased mobility of the soliton impedes the soliton to propagate at the critical velocity, which is necessary to maintain a constant power

at which a wave packet is neither amplified nor attenuated. In the linear regime, this velocity separates the attenuated parts of the Light Walk from the amplified (see Fig. 21), while in the nonlinear regime this velocity is a good approximation of the propagation angle of the dissipative soliton.

10 Solitons in the Global $\mathcal{PT}$-Symmetric Lattice

Already before the first study on linear beam dynamics in $\mathcal{PT}$-symmetrical systems [18], the first manuscript on $\mathcal{PT}$ solitons was published [53]. However, as the stringent requirements of $\mathcal{PT}$ symmetry on the used materials is even more restricted when including materials with a significant nonlinear response, $\mathcal{PT}$ solitons remained an exclusively theoretical topic for a long time[1] [53–66]. In this sense, the fiber network provides a versatile experimental platform for studying $\mathcal{PT}$ solitons [27].

In fact we could demonstrate nonlinearly induced localization and the formation of various solitons in the global $\mathcal{PT}$-symmetric fiber network (see Figs. 22 and 23). However, for a single side excitation as demonstrated in Fig. 22 solitons show a tendency of destabilization often resulting in a slight exponential power increase

[1]The list of references here does by far not provide a complete overview about the theoretical framework of $\mathcal{PT}$ solitons.

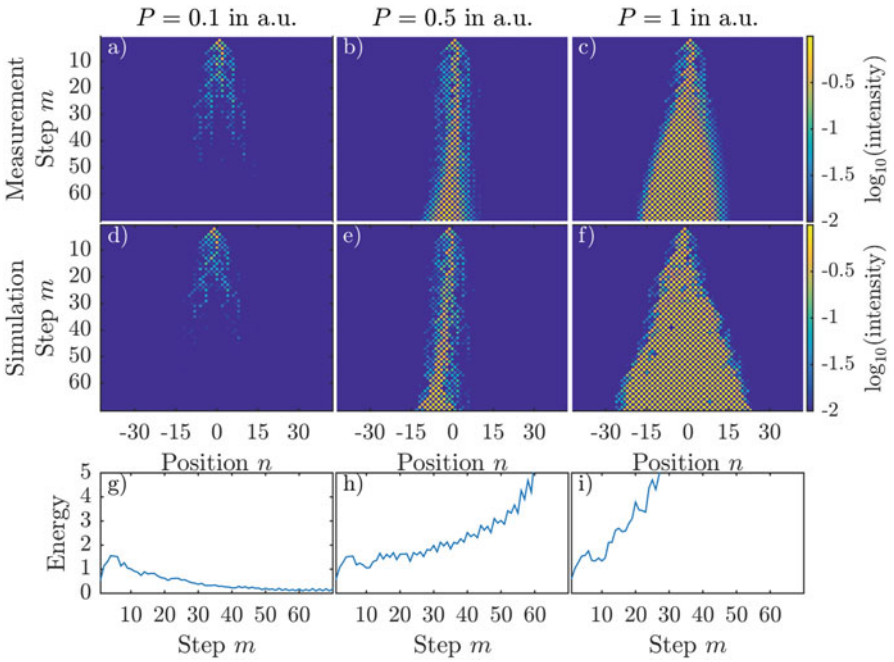

Fig. 22 Localization on the global $\mathcal{PT}$-symmetric lattice. By increasing the initial power, the spreading of a single lattice site excitation is strongly reduced until the wave packet clearly localizes. Due to the intrinsic instability of the $\mathcal{PT}$ lattice ($G = 2$, $\varphi = 0.4\pi$), nonlinear waves exponentially grow during propagation. By adding a global loss of 5% per round trip, the linear propagation is strongly damped, while only nonlinear waves survive, which acts like a saturable absorber. This figure is adapted from [27]

during propagation [26]. This is in stark contrast to an expected stabilizing effect of a focusing nonlinearity as predicted for continuous $\mathcal{PT}$-symmetric systems [66]. This instability seems to be an artifact of the discretization of the propagation in the mesh lattice. In the fiber network, phase and amplitude modulation as well as nonlinear propagation are strictly separated and thus seemingly more vulnerable with respect to perturbations. We utilized this idiosyncrasy in order to implement a saturable absorber. By adding global loss to the system, all linear waves are damped, but the soliton does not only pass the lossy system, but can be even additionally amplified during the propagation (see Fig. 22).

Besides the discrete localization, it is also possible to excite broad solitons in the global $\mathcal{PT}$-symmetric lattice with a Gaussian distribution. For these broad nonlinear waves, no intrinsic instability is visible. When increasing the amplitude of the Gaussian distribution, it self-focuses during the propagation and forms a soliton. As the input field is symmetric with respect to the real valued potential a sign change of the phase modulation $\varphi_0 \rightarrow -\varphi_0$ has a considerable impact on the propagation resulting in a transition from a single to a double hump soliton as shown in Fig. 23.

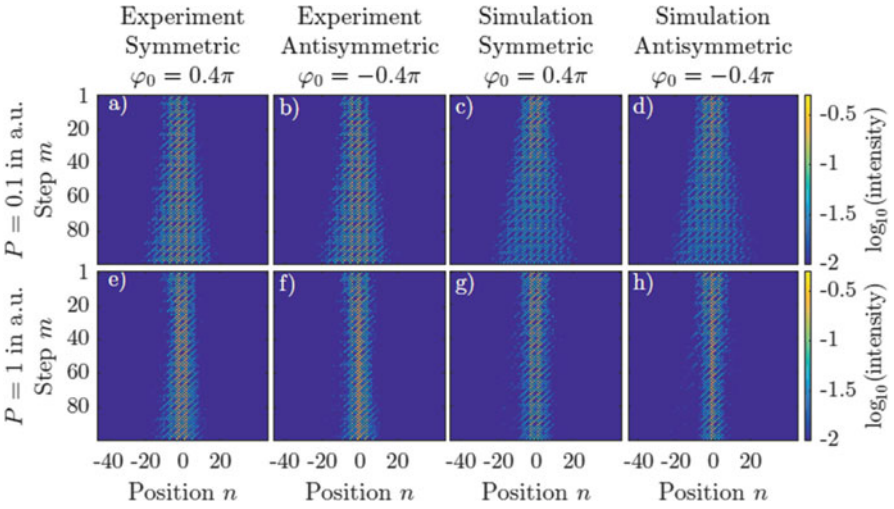

Fig. 23 Excitation of broad $\mathcal{PT}$ solitons in the experiment and simulation. In presence of gain and loss ($G = 1.4$) and a global phase modulation, broad solitons are excited, which show a stable propagation over 100 time steps in the experiment. By inverting the sign of the phase modulation, it is possible to change from a single to a double hump soliton. This figure is adapted from [27]

11 Conclusion

In the previous chapter we discussed linear and nonlinear light evolution in a synthetic photonic mesh lattice, where phase and amplitude modulators are used to establish $\mathcal{PT}$ symmetry. Based on the coupling of two fiber loops with a slight length imbalance, we showed how a double discrete $1 + 1$dimensional temporal system is created. Fiber amplifiers compensate for any losses and even allow, in combination with acousto-optical modulators, for dynamical variations of gain and loss in the network. By meticulously balancing the amplification and a suitable phase modulation, a $\mathcal{PT}$-symmetric lattice is synthesized. Although gain and loss are present, the band structure is completely real valued below the $\mathcal{PT}$ threshold. Furthermore, when combining the amplitude modulation with a phase gradient, Bloch oscillations are induced, which depict the dynamical wave propagation close to exceptional points as well as the existence of Bloch gradients featuring a pseudo-Hermitian propagation. In the local $\mathcal{PT}$-symmetric environment, we showed how to analyze the trajectories and amplitudes of wave packets performing Bloch oscillations in order to reconstruct real and imaginary part of the band structure.

In the limit of high power levels, we observe a clear localization of waves in the mesh lattice. While in the Hermitian system, a double discrete soliton forms, which is locked to a single lattice site, this soliton can be steered in the local $\mathcal{PT}$-symmetric environment via a global loss factor. The directionality of the gain/loss distribution leads to an effective cleaning of the soliton from perturbations as in convectively

stable nonlinear systems [49]. In the global $\mathcal{PT}$-symmetric mesh lattice, broad solitons are found, which propagate in a stable manner for over 100 time steps in the experiment. However, the $\mathcal{PT}$ symmetric mesh lattice seems to be intrinsically unstable with respect to nonlinear perturbations, which is demonstrated for single side excitations. In this case, the amplitudes of nonlinear waves drastically grow, which we in turn suppress by a global loss. In this case, a saturable absorber is formed, where linear waves are damped due to the global attenuation, while nonlinear waves propagate lossless or even with a net gain.

In the future, central topics in this research area will be the expansion to two spatial dimensions, as demonstrated in [10] for Quantum Walks, in combination with $\mathcal{PT}$ symmetry, as well as the merging of geometrical and topological effects with $\mathcal{PT}$ symmetry. For Bloch oscillations in $\mathcal{PT}$-symmetric systems precise measurements of the band structure were demonstrated. In combination with geometrical nontrivial systems [13], the same approach could provide useful insights into a non-Hermitian expansion of the concept of geometric phases. Additionally, higher dimensional systems provide direct access to the physics of exceptional rings [67].

Finally, by combining the phase and amplitude modulations, which both fulfill the requirements of $\mathcal{PT}$ symmetry, a pseudo-Hermitian propagation is established (see Fig. 9 fourth column), where even in the presence of gain and loss the total power stays constant on average. This is also highlighted by the dispersion relation, which is real valued for the entire Brillouin zone and free of any exceptional points [26] (see Fig. 7, fourth column). However, $\mathcal{PT}$ symmetry does not guarantee a real-valued dispersion relation as shown in Fig. 8. The band structure is only real for the gain parameter G below a critical threshold value, which depends on the amplitude φ_0 of the phase modulation. By either decreasing the phase potential φ_0 or by increasing the gain/loss imbalance above a critical value, it is possible to perform a transition across the $\mathcal{PT}$ threshold [26]. While parity and time symmetry are graphically illustrated in Fig. 6, an explicit and rigorous analysis of $\mathcal{PT}$ symmetry in the fiber network is provided in [30].

Acknowledgements We thank Alois Regensburger, Christoph Bersch, Georgy Onishchukov and Mohammad-Ali Miri for fruitful collaborations. Furthermore, we acknowledge financial support from the Erlangen Graduate School of Advanced Optical Technologies and GRK 2101.

References

1. Galton, F.: Natural Inheritance. Macmillan, New York (1889)
2. Kempe, J.: Quantum random walks: an introductory overview. Contemp. Phys. **44**, 307 (2003)
3. Bouwmeester, D., Marzoli, I., Karman, G.P., Schleich, W., Woerdman, J.P.: Optical Galton board. Phys. Rev. A. **61**, 13410 (1999)
4. Schreiber, A., Cassemiro, K.N., Potoček, V., Gábris, A., Jex, I., Silberhorn, C.: Decoherence and disorder in quantum walks: from ballistic spread to localization. Phys. Rev. Lett. **106**, 180403 (2011)

5. Karski, M., Forster, L., Choi, J.-M., Steffen, A., Alt, W., Meschede, D., Widera, A.: Quantum walk in position space with single optically trapped atoms. Science. **325**, 174 (2009)
6. Shenvi, N., Kempe, J., Whaley, K.B.: Quantum random-walk search algorithm. Phys. Rev. A. **67**, 52307 (2003)
7. Knight, P.L., Roldán, E., Sipe, J.E.: Quantum walk on the line as an interference phenomenon. Phys. Rev. A. **68**, 20301 (2003)
8. Schreiber, A., Cassemiro, K.N., Potoček, V., Gábris, A., Mosley, P.J., Andersson, E., Jex, I., Silberhorn, C.: Photons walking the line: a quantum walk with adjustable coin operations. Phys. Rev. Lett. **104**, 50502 (2010)
9. Kitagawa, T., Broome, M.A., Fedrizzi, A., Rudner, M.S., Berg, E., Kassal, I., Aspuru-Guzik, A., Demler, E., White, A.G.: Observation of topologically protected bound states in photonic quantum walks. Nat. Commun. **3**, 882 (2012)
10. Schreiber, A., Gabris, A., Rohde, P.P., Laiho, K., Stefanak, M., Potocek, V., Hamilton, C., Jex, I., Silberhorn, C.: A 2D quantum walk simulation of two-particle dynamics. Science. **336**, 55 (2012)
11. Regensburger, A., Bersch, C., Hinrichs, B., Onishchukov, G., Schreiber, A., Silberhorn, C., Peschel, U.: Photon propagation in a discrete fiber network: an interplay of coherence and losses. Phys. Rev. Lett. **107**, 233902 (2011)
12. Wimmer, M., Regensburger, A., Bersch, C., Miri, M., Batz, S., Onishchukov, G., Christodoulides, D.N., Peschel, U.: Optical diametric drive acceleration through action–reaction symmetry breaking. Nat. Phys. **9**, 780 (2013)
13. Wimmer, M., Price, H.M., Carusotto, I., Peschel, U.: Experimental measurement of the Berry curvature from anomalous transport. Nat. Phys. **13**, 545 (2017)
14. Gruner-Nielsen, L., Wandel, M., Kristensen, P., Jorgensen, C., Jorgensen, L.V., Edvold, B., Palsdottir, B., Jakobsen, D.: Dispersion-compensating fibers. J. Light. Technol. **23**, 3566 (2005)
15. Miri, M.-A., Regensburger, A., Peschel, U., Christodoulides, D.N.: Optical mesh lattices with *PT* symmetry. Phys. Rev. A. **86**, 23807 (2012)
16. Morandotti, R., Eisenberg, H.S., Silberberg, Y., Sorel, M., Aitchison, J.S.: Self-focusing and defocusing in waveguide arrays. Phys. Rev. Lett. **86**, 3296 (2001)
17. Bender, C.M., Boettcher, S.: Real spectra in non-hermitian hamiltonians having *PT* symmetry. Phys. Rev. Lett. **80**, 5243 (1998)
18. Makris, K.G., El-Ganainy, R., Christodoulides, D.N., Musslimani, Z.H.: Beam dynamics in *PT* symmetric optical lattices. Phys. Rev. Lett. **100**, 103904 (2008)
19. Guo, A., Salamo, G.J., Duchesne, D., Morandotti, R., Volatier-Ravat, M., Aimez, V., Siviloglou, G.A., Christodoulides, D.N.: Observation of *PT* -symmetry breaking in complex optical pot entials. Phys. Rev. Lett. **103**, 93902 (2009)
20. Weimann, S., Kremer, M., Plotnik, Y., Lumer, Y., Nolte, S., Makris, K.G., Segev, M., Rechtsman, M.C., Szameit, A.: Topologically protected bound states in photonic parity–time-symmetric crystals. Nat. Mater. **16**, 433 (2016)
21. Eichelkraut, T., Weimann, S., Stützer, S., Nolte, S., Szameit, A.: Radiation-loss management in modulated waveguides. Opt. Lett. **39**, 6831 (2014)
22. Xu, Y.-L., Fegadolli, W.S., Gan, L., Lu, M.-H., Liu, X.-P., Li, Z.-Y., Scherer, A., Chen, Y.-F.: Experimental realization of Bloch oscillations in a parity-time synthetic silicon photonic lattice. Nat. Commun. **7**, 11319 (2016)
23. Ornigotti, M., Szameit, A.: Quasi *PT* -symmetry in passive photonic lattices. J. Opt. **16**, 65501 (2014)
24. Peng, B., Özdemir, Ş.K., Lei, F., Monifi, F., Gianfreda, M., Long, G.L., Fan, S., Nori, F., Bender, C.M., Yang, L.: Parity–time-symmetric whispering-gallery microcavities. Nat. Phys. **10**, 394 (2014)
25. Hodaei, H., Miri, M.-A., Heinrich, M., Christodoulides, D.N., Khajavikhan, M.: Parity-time-symmetric microring lasers. Science. **346**, 975 (2014)
26. Regensburger, A., Bersch, C., Miri, M.A., Onishchukov, G., Christodoulides, D.N., Peschel, U.: Parity–time synthetic photonic lattices. Nature. **488**, 167 (2012)

27. Wimmer, M., Regensburger, A., Miri, M., Bersch, C., Christodoulides, D.N., Peschel, U.: Observation of optical solitons in PT-symmetric lattices. Nat. Commun. **6**, 7782 (2015)
28. Wimmer, M., Miri, M.-A., Christodoulides, D., Peschel, U.: Observation of Bloch oscillations in complex PT-symmetric photonic lattices. Sci. Rep. **5**, 17760 (2016)
29. Heiss, W.D.: The physics of exceptional points. J. Phys. A. Math. Theor. **45**, 444016 (2012)
30. Mochizuki, K., Kim, D., Obuse, H.: Explicit definition of *PT* symmetry for nonunitary quantum walks with gain and loss. Phys. Rev. A. **93**, 62116 (2016)
31. Longhi, S.: Bloch oscillations in complex crystals with *PT* symmetry. Phys. Rev. Lett. **103**, 123601 (2009)
32. Bloch, F.: Über die Quantenmechanik der Elektronen in Kristallgittern. Zeitschrift Für Phys. **52**, 555 (1929)
33. Zener, C.: A theory of the electrical breakdown of solid dielectrics. Proc. R. Soc. A. Math. Phys. Eng. Sci. **145**, 523 (1934)
34. Kittel, C.: Introduction into solid state physics, 8th edn. Wiley, New York (2005)
35. Peschel, U., Pertsch, T., Lederer, F.: Optical Bloch oscillations in waveguide arrays. Opt. Lett. **23**, 1701 (1998)
36. Pertsch, T., Dannberg, P., Elflein, W., Bräuer, A., Lederer, F.: Optical bloch oscillations in temperature tuned waveguide arrays. Phys. Rev. Lett. **83**, 4752 (1999)
37. Matjeschk, R., Ahlbrecht, A., Enderlein, M., Cedzich, C., Werner, A.H., Keyl, M., Schaetz, T., Werner, R.F.: Quantum walks with nonorthogonal position states. Phys. Rev. Lett. **109**, 240503 (2012)
38. Uzdin, R., Mailybaev, A., Moiseyev, N.: On the observability and asymmetry of adiabatic state flips generated by exceptional points. J. Phys. A Math. Theor. **44**, 435302 (2011)
39. Doppler, J., Mailybaev, A.A., Böhm, J., Kuhl, U., Girschik, A., Libisch, F., Milburn, T.J., Rabl, P., Moiseyev, N., Rotter, S.: Dynamically encircling an exceptional point for asymmetric mode switching. Nature. **537**, 76 (2016)
40. Mostafazadeh, A.: Invisibility and *PT* symmetry. Phys. Rev. A. **87**, 12103 (2013)
41. Longhi, S.: Invisibility in *PT* -symmetric complex crystals. J. Phys. A Math. Theor. **44**, 485302 (2011)
42. Lin, Z., Ramezani, H., Eichelkraut, T., Kottos, T., Cao, H., Christodoulides, D.N.: Unidirectional invisibility induced by PT-symmetric periodic structures. Phys. Rev. Lett. **106**, 213901 (2011)
43. Regensburger, A., Miri, M.-A., Bersch, C., Näger, J., Onishchukov, G., Christodoulides, D.N., Peschel, U.: Observation of defect states in *PT* -symmetric optical lattices. Phys. Rev. Lett. **110**, 223902 (2013)
44. Longhi, S.: Zak phase of photons in optical waveguide lattices. Opt. Lett. **39**, 1697 (2014)
45. Schomerus, H.: Topologically protected midgap states in complex photonic lattices. Opt. Lett. **38**, 1912 (2013)
46. Navarrete-Benlloch, C., Pérez, A., Roldán, E.: Nonlinear optical Galton board. Phys. Rev. A. **75**, 62333 (2007)
47. Kivshar, Y.S., Campbell, D.K.: Peierls-Nabarro potential barrier for highly localized nonlinear modes. Phys. Rev. E. **48**, 3077 (1993)
48. Morandotti, R., Eisenberg, H.S., Mandelik, D., Silberberg, Y., Modotto, D., Sorel, M., Stanley, C.R., Aitchison, J.S.: Interactions of discrete solitons with structural defects. Opt. Lett. **28**, 834 (2003)
49. Ankiewicz, A., Akhmediev, N.: Dissipative solitons: from optics to biology and medicine. Springer, Berlin/Heidelberg (2008)
50. Rozanov, N.N.: Dissipative optical solitons. Physics-Uspekhi. **43**, 421 (2000)
51. Akhmediev, N., Ankiewicz, A.: Dissipative solitons, pp. 1–17. Springer, Berlin/Heidelberg (2005)
52. Lederer, F., Stegeman, G.I., Christodoulides, D.N., Assanto, G., Segev, M., Silberberg, Y.: Discrete solitons in optics. Phys. Rep. **463**, 1 (2008)
53. Musslimani, Z.H., Makris, K.G., El-Ganainy, R., Christodoulides, D.N.: Optical solitons in *PT* periodic potentials. Phys. Rev. Lett. **100**, 30402 (2008)

54. He, Y., Zhu, X., Mihalache, D., Liu, J., Chen, Z.: Lattice solitons in *PT* -symmetric mixed linear-nonlinear optical lattices. Phys. Rev. A. **85**, 13831 (2012)
55. Miri, M.A., Aceves, A.B., Kottos, T., Kovanis, V., Christodoulides, D.N.: Bragg solitons in nonlinear PT-symmetric periodic potentials. Phys. Rev. A. **86**, 33801 (2012)
56. Li, C., Liu, H., Dong, L.: Multi-stable solitons in *PT* -symmetric optical lattices. Opt. Lett. **20**, 16823–16831 (2012)
57. Li, C., Huang, C., Liu, H., Dong, L.: Multipeaked gap solitons in PT-symmetric optical lattices. Opt. Lett. **37**, 4543 (2012)
58. Achilleos, V., Kevrekidis, P.G., Frantzeskakis, D.J., Carretero-González, R.: Dark solitons and vortices in *PT* -symmetric nonlinear media: From spontaneous symmetry breaking to nonlinear *PT* phase transitions. Phys. Rev. A. **86**, 13808 (2012)
59. Shi, Z., Jiang, X., Zhu, X., Li, H.: Bright spatial solitons in defocusing Kerr media with *PT* -symmetric potentials. Phys. Rev. A. **84**, 53855 (2011)
60. Abdullaev, F.K., Kartashov, Y.V., Konotop, V.V., Zezyulin, D.a.: Solitons in *PT* -symmetric nonlinear lattices. Phys. Rev. A. **83**, 41805 (2011)
61. Zhong, W.-P., Belić, M.R., Huang, T.: Two-dimensional accessible solitons in PT-symmetric potentials. Nonlinear Dyn. **70**, 2027 (2012)
62. Konotop, V.V., Pelinovsky, D.E., Zezyulin, D.A.: Discrete solitons in *PT* -symmetric lattices. EPL (Europhys. Lett.). **100**, 56006 (2012)
63. Nixon, S., Ge, L., Yang, J.: Stability analysis for solitons in *PT* -symmetric optical lattices. Phys. Rev. A. **85**, 23822 (2012)
64. Alexeeva, N.V., Barashenkov, I.V., Sukhorukov, A.a., Kivshar, Y.S.: Optical solitons in *PT* -symmetric nonlinear couplers with gain and loss. Phys. Rev. A. **85**, 63837 (2012)
65. Nixon, S., Zhu, Y., Yang, J.: Nonlinear dynamics of wave packets in parity-time-symmetric optical lattices near the phase transition point. Opt. Lett. **37**, 4874 (2012)
66. Lumer, Y., Plotnik, Y., Rechtsman, M.C., Segev, M.: Nonlinearly induced *PT* transition in photonic systems. Phys. Rev. Lett. **111**, 263901 (2013)
67. Zhen, B., Hsu, C.W., Igarashi, Y., Lu, L., Kaminer, I., Pick, A., Chua, S.-L., Joannopoulos, J.D., Soljačić, M.: Spawning rings of exceptional points out of Dirac cones. Nature. **525**, 354 (2015)